

---

# MONET: Multiview Semi-supervised Keypoint via Epipolar Divergence

---

Yasamin Jafarian\*

Yuan Yao\*

Hyun Soo Park

University of Minnesota  
{jafar026,yaoxx340,hspark}@umn.edu

## Abstract

This paper presents MONET—an end-to-end semi-supervised learning framework for a pose detector using multiview image streams. What differentiates MONET from existing models is its capability of detecting general subjects including non-human species without a pre-trained model. A key challenge of such subjects lies in the limited availability of expert manual annotations, which often leads to a large bias in the detection model. We address this challenge by using the epipolar constraint embedded in the unlabeled data in two ways. First, given a set of the labeled data, the keypoint trajectories can be reliably reconstructed in 3D using multiview optical flows, resulting in considerable data augmentation in space and time from nearly exhaustive views. Second, the detection across views must geometrically agree with each other. We introduce a new measure of geometric consistency in keypoint distributions called *epipolar divergence*—a generalized distance from the epipolar lines to the corresponding keypoint distribution. Epipolar divergence characterizes when two view keypoint distributions produces zero reprojection error. We design a twin network that minimizes the epipolar divergence through stereo rectification that can significantly alleviate computational complexity and sampling aliasing in training. We demonstrate that our framework can localize customized keypoints of diverse species, e.g., humans, dogs, and monkeys.

## 1 Introduction

With a few exceptions, modern designs of pose detectors [1–4] are, in theory, highly *flexible* to recognize any deformable articulated body pose with minor modifications. However, their uses are predominantly limited to human subjects due to the availability of a large training data (e.g., MS COCO [5] and MPII [6] that were manually annotated by crowd workers). This has been the significant impediment to build a general marker-less motion capture system for diverse subjects such as monkeys, mice, and dogs. Unlike human subjects, attaining equivalent sizable data for non-human species is infeasible due to the requirement of expert knowledge and larger intra-class variations (e.g., rhesus macaques vs. mandrill). Further, the keypoints are not customizable, or pre-defined by the existing datasets, which leads to challenges in applying it to computational behavioral study.

This paper addresses the core question in enabling flexible marker-less motion capture: “how do we build a keypoint detector that localizes customized poses with minimal manual effort?” We conjecture that the redundant visual information embedded in *unlabeled* synchronized multiview image streams can significantly alleviate these manual efforts and enhance the precision. This is possible because (1) the annotations can be augmented in space and time using multiview tracking<sup>2</sup>; (2) a large variation of visual appearance and pose caused by distinctive viewpoints can be generated using nearly exhaustive views; and (3) 3D geometric consistency across views can be enforced.

We present MONET (Multiview Optical Supervision Network)—an end-to-end semi-supervised learning framework for a pose detector of general subjects without a pre-trained model by leveraging

---

\*Both authors contributed equally to this work.

<sup>2</sup>An analogous approach has been used for a monocular camera that tracks an object bounding box [7].

unlabeled multiview image streams. The key insight is that the detection in one view can be deterministically transferred to another view via epipolar geometry [8], which allows a cross-view supervision. We introduce a new measure of geometric consistency in keypoint distributions called *epipolar divergence*—a generalized distance from the epipolar lines to the corresponding keypoint distribution. It characterizes when two view keypoint distributions produces zero reprojection error. We design a twin network that minimizes the epipolar divergence through stereo rectification that reduces computational complexity and sampling aliasing in training.

MONET takes as input synchronized multiview image streams with limited number of manual annotations ( $< 0.1\%$ ) and outputs a keypoint detection model. We reliably reconstruct the keypoint trajectories in 3D that produce considerable data augmentation in space and time for a subset of the unlabeled data ( $< 10\%$ ), and generate a multiview bootstrapping keypoint prior. We train the twin network to jointly minimize the keypoint detection error and reprojection error on both labeled and unlabeled data.

MONET is flexible: (1) keypoints can be customizable as it does not require a pre-trained model<sup>3</sup>, i.e., we train a detection model from scratch with manual annotations for each sequence; (2) it can build on any keypoint detector design such as DeepPose [4], CPM [2], and Hourglass [3], which localizes the keypoints through their distribution (heatmap); (3) it can apply to general multi-camera systems (e.g., different multi-camera rigs, number of cameras, and intrinsic parameters).

The main contributions include: (a) epipolar divergence that measures geometric consistency between two view keypoint distributions; (b) MONET design that efficiently minimizes the epipolar divergence via stereo rectification of the keypoint distributions; (c) large spatiotemporal data augmentation using 3D reconstruction of keypoint trajectories. We demonstrate that MONET is flexible to detect keypoints in various subjects (humans, dogs, and monkeys) in different camera rigs and that outperforms the existing baselines in terms of localization accuracy and precision (reprojection error).

## 2 Related Work

The physical and social behaviors of non-human species such as rhesus macaque monkeys has been widely used as a window to study human activities in neuroscience and psychology. While measuring their subtle behaviors in a form of 3D anatomic landmarks is key, implementing marker-based 3D tracking systems is challenging due to their sensitivity of reflective markers and occlusion by fur, which limits its application to heavily constrained body motion (e.g., body tied to a chair) [11]. Vision based marker-less motion capture is a viable solution to measure their free ranging behaviors [12–14].

In general, the number of 3D pose configurations of a deformable articulated body is exponential with respect to the number of joints. The 2D projections of the 3D body introduces another factor of variations (e.g., illumination, visual appearance, and occlusion) caused by viewpoint changes, which makes pose detection challenging. Yet, the pose configuration is often structured where efficient spatial representations such as pictorial structures [15–21] and graphical models [22–28] can alleviate the computational cost by using efficient algorithms, e.g., dynamic programming, convex relaxation, and approximate algorithms. Albeit efficient and accurate on iconic images, they exhibit inferior performance on the images in the long-tail distribution, e.g., a pigeon pose of yoga. Fully supervised learning frameworks using a millions of perceptrons in convolutional neural networks (CNN) [1–4] can address this long-tail distribution issue by leveraging a sheer amount of training data annotated by crowd workers [5, 6, 29]. However, due to the number of parameters in CNN, the trained model can be highly biased if the number of data samples is not sufficient ( $< 1M$ ).

Semi-supervised and weakly-supervised learning frameworks train CNN models with limited number of training data [30–41]. These approaches embed underlying spatial structures such as 3D skeletons and mesh that regularize their network weights. For instance, motion capture data are used to jointly learn 2D and 3D keypoints [31], and scanned human body models are used to validate 2D pose estimation via reprojection [42–46]. Notably, a multi-camera system can be used to cross-view supervise each other images using iterative process of 3D reconstruction and network training [47].

Unlike existing methods, MONET does not rely on a spatial model. To our best knowledge, this is the first paper that jointly reconstructs and trains a keypoint detector without the iterative processes using epipolar geometry. We integrate reconstruction and learning through a new measure of keypoint distributions called epipolar divergence, which can apply to general subjects including non-human species where minimal manual annotations are available.

---

<sup>3</sup>The existing models (e.g., AlexNet [9] and VGG 16 [10]) can be used as a complementary source to initialize the convolutional layers.

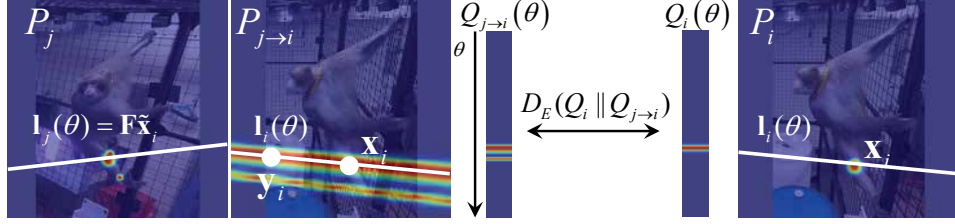


Figure 1: The keypoint distribution probability of the  $j^{\text{th}}$  image,  $P_j$ , can be transferred to the  $i^{\text{th}}$  image,  $P_{j \rightarrow i}(\mathbf{x}_i)$  by max-pooling along the epipolar line,  $\mathbf{F}\tilde{\mathbf{x}}_i$ . Note that the points that lie in an epipolar line have the same transferred probability,  $P_{j \rightarrow i}(\mathbf{x}_i) = P_{j \rightarrow i}(\mathbf{y}_i)$ . Epipolar divergence  $D_E(Q_i || Q_{j \rightarrow i})$  measures the distance between  $Q_{j \rightarrow i}(\theta)$  and  $Q_i(\theta)$ .

### 3 MONET: Multiview Optical Supervision Network

We present a semi-supervised learning framework for training a keypoint detection model by leveraging multiview image streams where  $|\mathcal{D}_U| \gg |\mathcal{D}_L|$  where  $\mathcal{D}_L$  and  $\mathcal{D}_U$  are labeled and unlabeled data. We design a twin network that enforces geometric consistency by minimizing epipolar divergence (Section 3.1 and 3.2), allowing a cross-view supervision. In addition, we extensively augment the labeled data by reconstructing 3D keypoint trajectories (Section 3.3), which provides a multiview bootstrapping prior (Section 3.4).

Consider a network model that takes an input image  $\mathcal{I}$  and outputs a keypoint distribution, i.e.,  $\phi(\mathcal{I}; \mathbf{w}) \in [0, 1]^{W \times H \times P}$  where  $W$  and  $H$  are the width and height of the keypoint distribution, respectively, and  $P$  is the number of keypoints. The network is parametrized by the weight  $\mathbf{w}$  learned by minimizing the following loss:

$$\underset{\mathbf{w}}{\text{minimize}} \quad \mathcal{L}_L + \lambda_e \mathcal{L}_E + \lambda_p \mathcal{L}_P, \quad (1)$$

where  $\mathcal{L}_L$ ,  $\mathcal{L}_E$ , and  $\mathcal{L}_P$  are the losses for labeled supervision, multiview cross-view supervision, and bootstrapping prior, and  $\lambda_e$  and  $\lambda_p$  are the weights that control their importance.

#### 3.1 Epipolar Divergence

A point in the  $i^{\text{th}}$  image  $\mathbf{x}_i \in \mathbb{R}^2$  is *transferred* to the corresponding epipolar line in the  $j^{\text{th}}$  image via the fundamental matrix  $\mathbf{F}$  between two relative camera poses, which measures geometric consistency, i.e., the corresponding point  $\mathbf{x}_j$  must lie in the epipolar line [8]:

$$D(\mathbf{x}_i, \mathbf{x}_j) = |\tilde{\mathbf{x}}_j^\top (\mathbf{F}\tilde{\mathbf{x}}_i)| \propto \inf_{\mathbf{x} \in \mathbf{F}\tilde{\mathbf{x}}_i} \|\mathbf{x} - \mathbf{x}_j\|, \quad (2)$$

where  $\tilde{\mathbf{x}}$  is the homogeneous representation of  $\mathbf{x}$ . Equation (2) measures the closest distance between  $\mathbf{x}_j$  and all points that lies in the epipolar line  $\mathbf{F}\tilde{\mathbf{x}}_i$ , i.e., the distance between line and point.

We generalize the epipolar line transfer to define the distance between keypoint distributions. Let  $P_i : \mathbb{R}^2 \rightarrow [0, 1]$  be the probability distribution given the  $i^{\text{th}}$  image computed by the keypoint detector, i.e.,  $P_i(\mathbf{x}) = \phi(\mathcal{I}_i; \mathbf{w})|_{\mathbf{x}}$ , and  $P_{j \rightarrow i} : \mathbb{R}^2 \rightarrow [0, 1]$  be the probability distribution in the  $i^{\text{th}}$  image *transferred* from the  $j^{\text{th}}$  image. Note that we use an abuse of notation by omitting the keypoint index as each keypoint is considered independently.

Consider a line max-pooling operation  $g$ :

$$g(\mathbf{l}; P) = \sup_{\mathbf{x} \in \mathbf{l}} P(\mathbf{x}), \quad (3)$$

where  $P : \mathbb{R}^2 \rightarrow [0, 1]$  is a probability distribution and  $\mathbf{l} \in \mathbb{P}^2$  is a 2D line parameter.  $g$  takes the maximum value along the line in  $P$ . Given the keypoint distribution in the  $j^{\text{th}}$  image  $P_j$ , the transferred keypoint distribution can be obtained:

$$P_{j \rightarrow i}(\mathbf{x}_i) = g(\mathbf{F}\tilde{\mathbf{x}}_i; P_j). \quad (4)$$

The supremum operation is equivalent to the infimum operation in Equation (2) where it finds the most likely (closest) correspondences along the epipolar line. The first two images in Figure 1 illustrates the keypoint distribution transfer via Equation (4). It is the projection of a posteriori distribution of a 3D keypoint generated by the  $j^{\text{th}}$  image onto the  $i^{\text{th}}$  image given an uniform prior distribution.  $P_i$  and  $P_{j \rightarrow i}$  cannot be matched because  $P_i$  is a point distribution while  $P_{j \rightarrow i}$  is a line distribution.

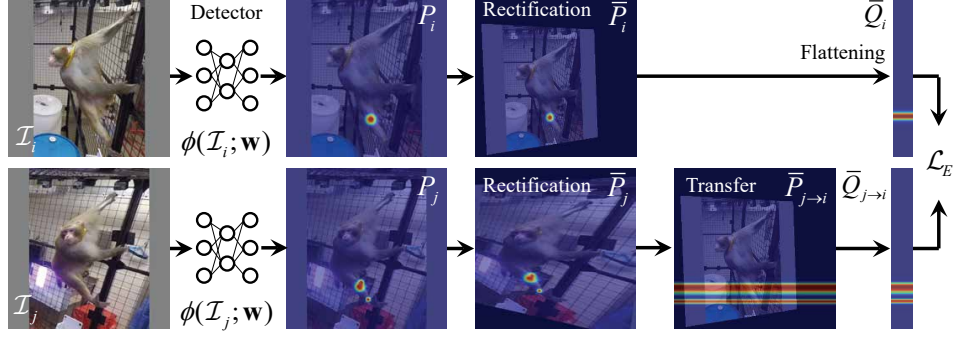


Figure 2: We design a twin network to minimize the epipolar divergence between  $\bar{Q}_i$  and  $\bar{Q}_{j \rightarrow i}$ . Stereo rectification is used to simplify the max-pooling operation along the epipolar line, which reduces computational complexity and sampling aliasing.

Note that in  $P_{j \rightarrow i}$ , a family of points that lie in an epipolar line share the same probability because they all map to a single epipolar line in the other image, i.e.,  $P_{i \rightarrow j}(\mathbf{x}_j) = P_{i \rightarrow j}(\mathbf{y}_j)$  if  $\mathbf{F}^\top \tilde{\mathbf{x}}_j \propto \mathbf{F}^\top \tilde{\mathbf{y}}_j$  as shown in the second image of Figure 1. This indicates that the transferred probability distribution can be parametrized by the slope of an epipolar line,  $\theta \in \mathbb{S}$ , i.e.,

$$Q_{j \rightarrow i}(\theta) = g(\mathbf{l}_i(\theta); P_{j \rightarrow i}), \quad (5)$$

where  $\mathbf{l}_i(\theta)$  is the line passing through the epipole parametrized by  $\theta$  in the  $i^{\text{th}}$  image, and  $Q_{j \rightarrow i} : \mathbb{S} \rightarrow [0, 1]$  is a flattened 1D distribution across the line. Similarly, the flattened keypoint distribution of  $P_i$  can be defined as  $Q_i(\theta) = g(\mathbf{l}_i(\theta); P_i)$ .

**Theorem 1.** Two keypoint distributions  $P_i$  and  $P_j$  are geometrically consistent, i.e., zero reprojection error, if  $Q_i(\theta) = Q_{j \rightarrow i}(\theta)$ .

See the proof in Appendix A. Based on the Theorem 1, we match  $Q_i$  and  $Q_{j \rightarrow i}$ . Inspired by KL divergence [48], we define *epipolar divergence* that measures the difference between two keypoint distributions mapped by their fundamental matrix using relative entropy:

$$D_E(Q_i || Q_{j \rightarrow i}) = \int_{\mathbb{S}} Q_i(\theta) \log \frac{Q_i(\theta)}{Q_{j \rightarrow i}(\theta)} d\theta, \quad (6)$$

where  $D_E$  is epipolar divergence, i.e., how two keypoint distributions are geometrically consistent.

### 3.2 Cross-view Supervision via Epipolar Divergence

In practice, embedding Equation (6) into an end-to-end neural network is not trivial because (a) a new max-pooling operation over oblique epipolar lines in Equation (4) needs to be defined; (b) sampling interval for max-pooling along the line is arbitrary, i.e., uniform sampling does not encode geometric meaning such as depth; and (c) sampling interval across  $\theta$  is also arbitrary, which introduces sampling aliasing. This leads to irregular keypoint distribution transfer based on the fundamental matrix.

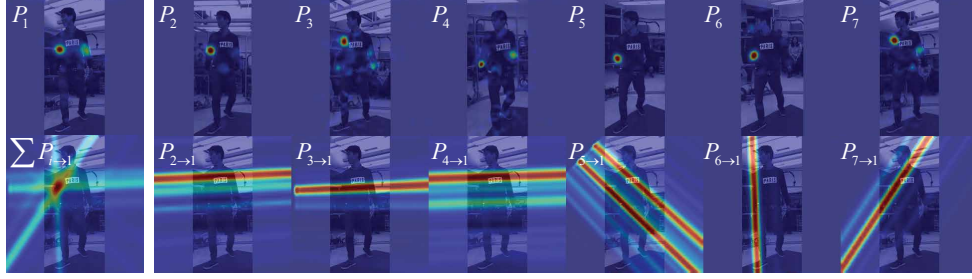
We introduce a new operation inspired by stereo rectification, which warps the keypoint distribution such that the epipole is transformed to a point at infinity, i.e., the epipolar lines become parallel (horizontal) as shown the bottom right image in Figure 2. This rectification allows converting the oblique line max-pooling into regular row-wise max-pooling. Equation (3) can be re-written in the rectified keypoint distribution:

$$\bar{g}(v; \bar{P}) = g\left(\mathbf{l}(v) = \begin{bmatrix} 0 \\ -1/v \\ 1 \end{bmatrix}; \bar{P}\right) = \max_u \bar{P}\left(\mathbf{x} = \begin{bmatrix} u \\ v \end{bmatrix}\right) \quad (7)$$

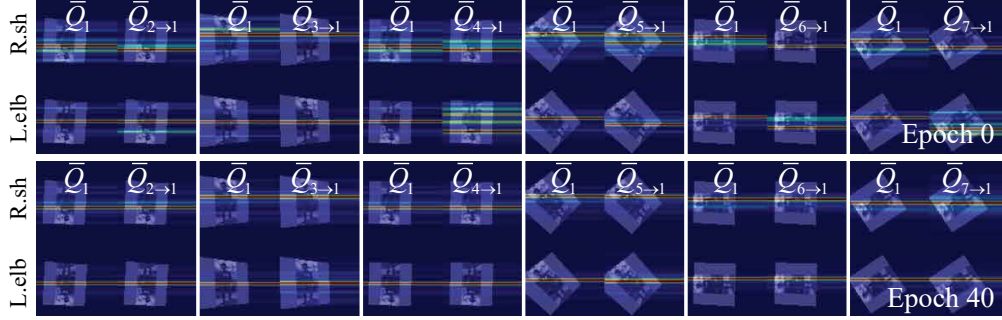
where  $(u, v)$  are the  $x, y$ -coordinate of a point in the rectified keypoint distribution warped from  $P$ , i.e.,  $\bar{P}(\mathbf{x}) = P(\mathbf{H}_r^{-1}\mathbf{x})$  where  $\mathbf{H}_r$  is a homography of stereo-rectification.  $\bar{P}$  is computed by inverse homography warping with bilinear interpolation [49, 50].

This rectification simplifies the flattening operation in Equation (5):

$$\bar{Q}_{j \rightarrow i}(v) = \bar{g}(v; \bar{P}_{j \rightarrow i}) = \bar{g}(av + b; \bar{P}_j), \quad \bar{Q}_i(v) = \bar{g}(v; \bar{P}_i), \quad (8)$$



(a) Epipolar cross-view supervision on right elbow



(b) Convergence of epipolar divergence

Figure 3: (a) We use multiple images to supervise the keypoint distribution, e.g.,  $P_1$  is cross-view supervised by  $P_2, \dots, P_7$ . The bottom left image is the summation of cross-view supervisions. (b) The twin network minimizes epipolar divergence:  $\bar{Q}_1$  and  $\bar{Q}_{j \rightarrow 1}$  are overlaid with stereo rectified images of right shoulder (R.sh) and left elbow (L.elb), which becomes horizontally aligned through training.

where  $a$  and  $b$  are re-scaling factors between the  $i^{\text{th}}$  and  $j^{\text{th}}$  cameras accounting different camera intrinsic and cropping parameters. See Appendix B for more details.

The key innovation of Equation (8) is that  $\bar{Q}_{j \rightarrow i}(v)$  is no longer parametrized by  $\theta$  where an additional sampling over  $\theta$  is not necessary. It directly accesses to  $\bar{P}_j$  to max-pool over each row, which significantly alleviates the computational complexity and sampling aliasing. Moreover, the sampling over  $x$ -coordinate is geometrically meaningful, i.e., uniform sampling is equivalent to disparity, or inverse depth.

With the rectification, we model the loss for multiview cross-view supervision:

$$\mathcal{L}_E = \sum_{p=1}^P \sum_{i=1}^C \sum_{j \in \mathcal{V}_i} \sum_{v=1}^H \bar{Q}_i(v) \log \frac{\bar{Q}_i^p(v)}{\bar{Q}_{j \rightarrow i}^p(v)} \quad (9)$$

where  $H$  is the height of the distribution,  $P$  is the number of keypoints,  $C$  is the number of cameras,  $\mathcal{V}_i$  is the set of paired camera indices of the  $i^{\text{th}}$  camera. We use the superscript in  $\bar{Q}_i^p$  to indicate the keypoint index. Figure 2 illustrates our twin network that minimizes the epipolar divergence by applying stereo rectification, epipolar transfer, and flattening operations, which can cross-view supervise the unlabeled data.

Since the epipolar divergence flattens the keypoint distribution, a pair of images can supervise along one direction. In practice, we find a set of paired image given  $i^{\text{th}}$  image such that the expected epipolar lines are not parallel as shown in Figure 3(a). When camera centers lie in a co-planar surface, a 3D point in the surface produces all same epipolar lines, which is a degenerate case<sup>4</sup>. Figure 3(b) illustrate how the twin network minimizes the epipolar divergence where  $\bar{Q}_1$  becomes aligned with  $\bar{Q}_{j \rightarrow 1}$  as training epoch increases.

### 3.3 Multiview Data Augmentation

We augment the labeled data by reconstructing the 3D keypoint trajectories using multiview image streams. Given synchronized labeled images, we triangulate each 3D keypoint  $\mathbf{X}$  using camera

<sup>4</sup>This degenerate case does not apply for 3D point triangulation where the correspondence is known.

projection matrix and the 2D labeled keypoints. The 3D reconstructed keypoint can be projected to the rest synchronized unlabeled images, which automatically produces their labels. 3D tracking [51, 52] can further increase the labeled data. For each keypoint  $\mathbf{X}_t$  at the  $t$  time instant, we project the point onto the visible set of cameras. The projected point is tracked in 2D using optical flow and triangulated with RANSAC [53] to form  $\mathbf{X}_{t+1}$ . We precisely compute the visibility of the point to reduce tracking drift using motion and appearance cues: (1) optical flow on each image is compared to the projected 3D motion vector to measure motion consistency; and (2) visual appearance is matched by learning a linear correlation filter [54] on PCA HOG [55], which can reliably track longer than 100 frames forward and backward. We use this spatiotemporal data augmentation to define the labeled data loss:

$$\mathcal{L}_L = \sum_{i \in \mathcal{D}_L} \|\phi(\mathcal{I}_i; \mathbf{w}) - \mathbf{z}_i\|^2 \quad (10)$$

where  $\mathbf{z} \in [0, 1]^{W \times H \times P}$  is the labeled likelihood of keypoints approximated by convolving the keypoint location with a Gaussian kernel.

### 3.4 Bootstrapping Prior

Multiview bootstrapping [47] can be used to generate the pseudo-labeled data via 3D triangulation via RANSAC. We initialize the detection model  $\mathbf{w}_0$  using the labeled data and filter the noisy detected keypoints using RANSAC conditioned on their detection probability. We use the projection of the reconstructed keypoint to generate a keypoint pseudo-probability map,  $\hat{\mathbf{z}} \in [0, 1]^{W \times H \times P}$ . We penalize the deviation from the bootstrapping prior:

$$\mathcal{L}_P = \sum_{i \in \mathcal{D}_U} \|\phi(\mathcal{I}_i; \mathbf{w}) - \hat{\mathbf{z}}_i\|^2. \quad (11)$$

Unlike hard labeling using pseudo-probability [47], our prior loss balances with the multiview cross-view supervision, which shows superior performance.

## 4 Result

We validate our MONET framework on multiple sequences of diverse subjects, humans, dogs, and monkeys, with two different multi-camera systems. A subset of images (4~5 images per frame) is manually annotated<sup>5</sup> over 10~20 frames (total annotated images per sequence is less than 100). Such manual annotations constitute 0.07%~0.14% of the unlabeled data. Human and dog subjects are captured by 69 cameras, and monkey subjects are captured by 35 cameras. See more details in Appendix C. To evaluate the flexibility, we build a model per species without a pre-trained model. The CPM network with 5 stages is used to build the twin network, and  $\lambda_e = 5$  and  $\lambda_p = 1$  are used.

We compare our approach with 5 different baseline algorithms. For all algorithms, we evaluate the performance on the unlabeled data. (1) **No augmentation**: we use the manually annotated images to train the network. Due to the limited number of labeled images ( $< 100$ ), the existing distillation methods [56, 57] perform similarly. (2) **Spatial augmentation**: the 3D keypoints are triangulated and projected onto the synchronized unlabeled images. This can model the visual appearance and spatial configuration from multiple perspectives, which can greatly improve the generalization power of the keypoint detection. (3) **Spatiotemporal augmentation**: we track the 3D keypoints over time using multiview optical flow [51, 52]. This augmentation can model different geometric configurations of 3D keypoints. (4) **Bootstrapping I**: Given the spatiotemporal data augmentation, we apply the multiview bootstrapping approach [47] to attain the pseudo-labels computed by RANSAC based 3D triangulation for the unlabeled data. (5) **Bootstrapping II**: the Bootstrapping I model can be refined by re-triangulation and re-training. This can reduce the reprojection errors. We evaluate our approach based on accuracy and precision: accuracy measures distance from the ground truth keypoint and precision measures the coherence of keypoint detection across views.

**Accuracy** We use PCK (probability of correct keypoint) curves to measure the accuracy. The distance between the ground truth keypoint and the detected keypoint is normalized by the size of the width of the detection window (46). Figure 4 shows PCK performance on human, monkey, and dog subjects where no pre-trained model is used. Our MONET (red) model exhibits accurate detection for all keypoints, which outperforms 5 baselines. For the monkey data, higher framerate image streams (60 fps) greatly boost the performance of multiview tracking due to small displacement, resulting in accurate keypoint detection by spatiotemporal augmentation.

<sup>5</sup>Exceptionally, for human subjects, pre-trained CPM model [1] is used to generate the ground truth data.



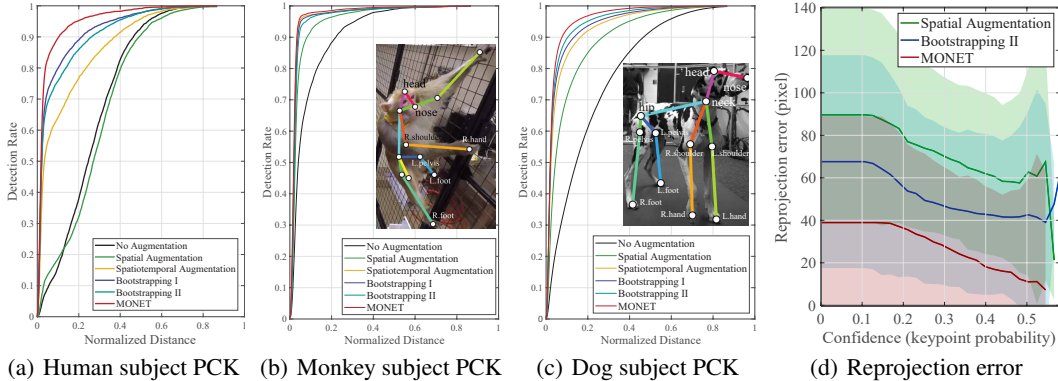


Figure 4: PCK curves for (a) humans, (b) monkeys, and (c) dogs. Our MONET (red) outperforms 5 baseline algorithms. (d) Our MONET is designed to minimize the reprojection error where we achieve far stronger performance as the confidence increases.

**Precision** We use reprojection error to evaluate the precision of the detection. Given a set of keypoint detections in a synchronized frame and 3D camera poses, we triangulate the 3D point without RANSAC. The 3D point is

projected back to each camera to compute the reprojection error, which measures geometric consistency across all views. Our MONET is designed to minimize the reprojection error where it outperforms the baselines with large margin as shown in Figure 4(d), showing the reprojection error with respect to keypoint probability. Our MONET performs better at higher keypoint probability, which is key for 3D reconstruction because it indicates which point to triangulate. The performance for each subject is summarized in Table 1.

	Human subject	Monkey subject	Dog subject
No aug.	77.8±73.3 (57.4)	31.1±872 (9.87)	88.9±69.9 (71.7)
Spatial aug.	69.0±66.2 (50.3)	12.9±26.6 (5.81)	37.5±47.1 (22.2)
Spatiotemporal aug.	50.3±65.4 (28.3)	8.10±17.8 (4.55)	24.0±36.2 (12.9)
Bootstrapping I	28.5±44.7 (15.2)	8.68±18.9 (4.71)	18.9±31.0 (9.86)
Bootstrapping II	35.4±62.4 (16.3)	9.97±22.1 (5.07)	17.1±29.3 (9.02)
MONET	<b>15.0±24.1 (10.0)</b>	<b>5.45±11.4 (3.63)</b>	<b>10.6±18.0 (6.75)</b>

Table 1: Reprojection error. Mean±Std (Median)

**Qualitative comparison** The qualitative comparison can be found in Figure 6. MONET precisely localize keypoints by leveraging multiview images jointly. This becomes more evident when disambiguating symmetric keypoints, e.g., left and right hands, as epipolar divergence penalizes geometric inconsistency, i.e., reprojection error. Also it shows stronger performance on occlusion (the bottom figure) as the occluded keypoints can be visible to other view images that can enforce to the correct location. Figure 5 illustrates 3D reconstruction of monkey movement using MONET.

## 5 Discussion

We present a new semi-supervised framework MONET to train a keypoint detection network by leveraging multiview image streams. The key innovation is a measure of geometric consistency of two keypoint distributions called epipolar divergence. Similar to epipolar distance between corresponding points, it allows us to directly compute the reprojection error while training the network. We introduce a stereo rectification of the keypoint distribution that simplifies the computational complexity and imposes geometric meaning on constructing 1D distributions. A twin network is used to embed computing epipolar divergence. We also use multiview image streams to augment the data in space and time, which can bootstrap the unlabeled data. We demonstrate that our framework outperforms existing approaches, e.g., multiview bootstrapping, in terms of accuracy (PCK) and precision (reprojection error) and apply to track non-human species such as dogs and monkeys. We anticipate that this framework will provide a fundamental basis for enabling a *flexible* markerless motion capture that requires exploiting a large (potentially infinite) number of unlabeled data.

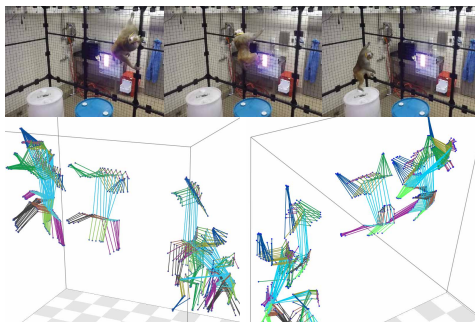


Figure 5: 3D reconstruction of a monkey subject.



Figure 6: We qualitatively compare our MONET with 5 baseline algorithms on humans, monkeys, and dogs.



## References

- [1] Z. Cao, T. Simon, S.-E. Wei, and Y. Sheikh, "Realtime multi-person 2d pose estimation using part affinity fields," in *CVPR*, 2017.
- [2] S.-E. Wei, V. Ramakrishna, T. Kanade, and Y. Sheikh, "Convolutional pose machines," in *CVPR*, 2016.
- [3] A. Newell, K. Yang, and J. Deng, "Stacked hourglass networks for human pose estimation," in *ECCV*, 2016.
- [4] A. Toshev and C. Szegedy, "DeepPose: Human pose estimation via deep neural networks," in *CVPR*, 2014.
- [5] T.-Y. Lin, M. Maire, S. Belongie, J. Hays, P. Perona, D. Ramanan, P. Dollár, and C. L. Zitnick, "Microsoft coco: Common objects in context," in *ECCV*, 2014.
- [6] M. Andriluka, L. Pishchulin, P. Gehler, and B. Schiele, "2d human pose estimation: New benchmark and state of the art analysis," in *CVPR*, 2014.
- [7] X. Wang and A. Gupta, "Unsupervised learning of visual representations using videos," in *ICCV*, 2015.
- [8] R. Hartley and A. Zisserman, *Multiple View Geometry in Computer Vision*. Cambridge University Press, second ed., 2004.
- [9] A. Krizhevsky, I. Sutskever, and G. E. Hinton, "Imagenet classification with deep convolutional neural networks," in *NIPS*, 2012.
- [10] K. Simonyan and A. Zisserman, "Very deep convolutional networks for large-scale image recognition," in *arXiv:1409.1556*, 2014.
- [11] A. D. M., "The nonhuman primate as a model for biomedical research," *Sourcebook of Models for Biomedical Research*, 2008.
- [12] J. D. Foster, P. Nuyujukian, O. Freifeld, H. Gao, R. Walker, S. I. Ryu, T. H. Meng, B. Murmann, M. J. Black, and K. V. Shenoy, "A freely-moving monkey treadmill model," *Journal of Neural Engineering*, 2014.
- [13] W. I. Sellers and E. Hirasaki, "Markerless 3d motion capture for animal locomotion studies," *Biology Open*, 2014.
- [14] T. Nakamura, J. Matsumoto, H. Nishimaru, R. V. Bretas, Y. Takamura, E. Hori, T. Ono, and H. Nishijo, "A markerless 3d computerized motion capture system incorporating a skeleton model for monkeys," *Plos ONE*, 2016.
- [15] M. Andriluka, S. Roth, and B. Schiele, "Monocular 3d pose estimation and tracking by detection," in *CVPR*, 2010.
- [16] M. Andriluka, S. Roth, and B. Schiele, "Pictorial structures revisited: People detection and articulated pose estimation," in *CVPR*, 2009.
- [17] P. Felzenszwalb and D. Huttenlocher, "Pictorial structures for object recognition," *IJCV*, 2005.
- [18] S. Johnson and M. Everingham, "Clustered pose and nonlinear appearance models for human pose estimation," in *BMVC*, 2010.
- [19] L. Pishchulin, M. Andriluka, P. Gehler, and B. Schiele, "Poselet conditioned pictorial structures," in *CVPR*, 2013.
- [20] L. Pishchulin, M. Andriluka, P. Gehler, and B. Schiele, "Strong appearance and expressive spatial models for human pose estimation," in *ICCV*, 2013.
- [21] Y. Yang and D. Ramanan, "Articulated pose estimation with flexible mixtures-of-parts," in *CVPR*, 2011.
- [22] M. Sun and S. Savarese, "Articulated part-based model for joint object detection and pose estimation," in *ICCV*, 2011.
- [23] Y. Tian, C. L. Zitnick, and S. G. Narasimhan, "Exploring the spatial hierarchy of mixture models for human pose estimation," in *ECCV*, 2012.
- [24] M. Dantone, J. Gall, C. Leistner, and L. V. Gool, "Human pose estimation using body parts dependent joint regressors," in *CVPR*, 2013.
- [25] L. Karlinsky and S. Ullman, "Using linking features in learning non-parametric part models," in *ECCV*, 2012.
- [26] X. Lan and D. Huttenlocher, "Beyond trees: Common-factor models for 2d human pose recovery," in *ICCV*, 2005.
- [27] L. Sigal and M. Black, "Measure locally, reason globally: Occlusion-sensitive articulated pose estimation," in *CVPR*, 2006.
- [28] Y. Wang and G. Mori, "Multiple tree models for occlusion and spatial constraints in human pose estimation," in *ECCV*, 2008.
- [29] J. Shotton, A. Fitzgibbon, M. Cook, T. Sharp, M. Finocchio, R. Moore, A. Kipman, and A. Blake, "Real-time human pose recognition in parts from single depth images," in *CVPR*, 2011.

- [30] N. Ukita and Y. Uematsu, "Semi- and weakly-supervised human pose estimation," in *CVIU*, 2018.
- [31] X. Zhou, Q. Huang, X. Sun, X. Xue, and Y. Wei, "Towards 3d human pose estimation in the wild: a weakly-supervised approach," in *ICCV*, 2017.
- [32] V. Belagiannis, S. Amin, M. Andriluka, B. Schiele, N. Navab, and S. Ilic, "3d pictorial structures revisited: Multiple human pose estimation," *TPAMI*, 2016.
- [33] B. Tekin, A. Rozantsev, V. Lepetit, and P. Fua, "Direct prediction of 3d body poses from motion compensated sequences," in *CVPR*, 2016.
- [34] V. Liang, K. Gong, X. Shen, and L. Lin, "Look into person: Joint body parsing & pose estimation network and a new benchmark," *TPAMI*, 2018.
- [35] U. Iqbal, A. Milan, and J. Gall, "Posetrack: Joint multi-person pose estimation and tracking," in *CVPR*, 2017.
- [36] S. Park, B. X. Nie, and S.-C. Zhu, "Attribute and-or grammar for joint parsing of human pose, parts and attributes," *TPAMI*, 2017.
- [37] B. Liu and V. Ferrari, "Active learning for human pose estimation," in *CVPR*, 2017.
- [38] M. Lin, L. Lin, and X. Liang, "Recurrent 3d pose sequence machines," in *CVPR*, 2017.
- [39] G. Pavlakos, X. Zhou, K. G. Derpanis, and K. Daniilidis, "Harvesting multiple views for marker-less 3d human pose annotations," in *CVPR*, 2017.
- [40] J. Song, L. Wang, L. V. Gool, and O. Hilliges, "Thin-slicing network: A deep structured model for pose estimation in videos," in *CVPR*, 2017.
- [41] F. Moreno-Noguer, "3d human pose estimation from a single image via distance matrix regression," in *CVPR*, 2017.
- [42] R. A. Guler, N. Neverova, and I. Kokkinos, "Densepose: Dense human pose estimation in the wild," in *CVPR*, 2018.
- [43] H. Joo, T. Simon, and Y. Sheikh, "Total capture: A 3d deformation model for tracking faces, hands, and bodies," in *CVPR*, 2018.
- [44] A. Kanazawa, M. J. Black, D. W. Jacobs, and J. Malik, "End-to-end recovery of human shape and pose," in *CVPR*, 2017.
- [45] T. Yu, Z. Zheng, K. Guo, J. Zhao, Q. Dai, H. Li, G. Pons-Moll, and Y. Liu, "Doublefusion: Real-time capture of human performances with inner body shapes from a single depth sensor," in *CVPR*, 2018.
- [46] S. Zuffi, A. Kanazawa, D. Jacobs, and M. J. Black, "3d menagerie: Modeling the 3d shape and pose of animals," in *CVPR*, 2017.
- [47] T. Simon, H. Joo, I. Matthews, and Y. Sheikh, "Hand keypoint detection in single images using multiview bootstrapping," in *CVPR*, 2017.
- [48] S. Kullback and R. A. Leibler, "On information and sufficiency," *Annals of Mathematical Statistics*, 1951.
- [49] M. Jaderberg, K. Simonyan, A. Zisserman, and K. Kavukcuoglu, "Spatial transformer networks," in *NIPS*, 2015.
- [50] K. He, G. Gkioxari, P. Dollar, and R. Girshick, "Mask r-cnn," in *CVPR*, 2017.
- [51] H. Joo, H. S. Park, and Y. Sheikh, "Map visibility estimation for large-scale dynamic 3d reconstruction," in *CVPR*, 2014.
- [52] J. S. Yoon, Z. Li, and H. S. Park, "3d semantic trajectory reconstruction from 3d pixel continuum," in *CVPR*, 2018.
- [53] M. A. Fischler and R. C. Bolles, "Random sample consensus: A paradigm for model fitting with applications to image analysis and automated cartography," *ACM Comm.*, 1981.
- [54] V. N. Boddeti and B. V. Kumar, "A framework for binding and retrieving class-specific information to and from image patterns using correlation filters," *TPAMI*, 2013.
- [55] N. Dalal and B. Triggs, "Histograms of oriented gradients for human detection," in *CVPR*, 2005.
- [56] O. V. G. Hinton and J. Dean, "Distilling the knowledge in a neural network," in *arXiv:1503.02531*, 2015.
- [57] I. Radosavovic, P. Dollár, R. Girshick, G. Gkioxari, and K. He, "Data distillation: Towards omni-supervised learning," in *arXiv:1712.04440*, 2017.
- [58] J. F. Henriques, R. Caseiro, P. Martins, and J. Batista, "High-speed tracking with kernelized correlation filters," *TPAMI*, 2015.

## A Proof of Theorem 1

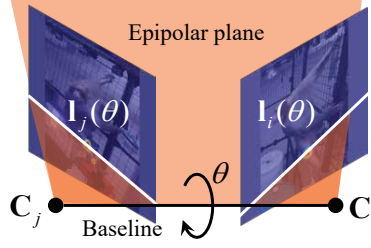


Figure 7: Two epipolar lines are induced by an epipolar plane, which can be parametrized by the rotation  $\theta$  about the baseline where  $\mathbf{C}_i$  and  $\mathbf{C}_j$  are the camera optical centers.

*Proof.* The geometric consistency, or zero reprojection error, is equivalent to proving  $\mathbf{L}_i^*, \mathbf{L}_j^* \in \Pi$  where  $\Pi$  is an epipolar plane rotating about the camera baseline  $\overline{\mathbf{C}_i\mathbf{C}_j}$  as shown in Figure 7, and  $\mathbf{L}_i^*$  and  $\mathbf{L}_j^*$  are the 3D rays produced by the inverse projection of correspondences  $\mathbf{x}_i^* \leftrightarrow \mathbf{x}_j^*$ , respectively, i.e.,  $\mathbf{L}_i^* = \mathbf{C}_i + \lambda \mathbf{R}_i^\top \mathbf{K}^{-1} \tilde{\mathbf{x}}_i^*$ . The correspondence from the keypoint distributions are:

$$\mathbf{x}_i^* = \underset{\mathbf{x}}{\operatorname{argmax}} P_i(\mathbf{x}) \quad (12)$$

$$\mathbf{x}_j^* = \underset{\mathbf{x}}{\operatorname{argmax}} P_j(\mathbf{x}), \quad (13)$$

$Q_i(\theta) = Q_{j \rightarrow i}(\theta)$  implies:

$$\begin{aligned} \theta^* &= \underset{\theta}{\operatorname{argmax}} \sup_{\mathbf{x} \in l_i(\theta)} P_i(\mathbf{x}) \\ &= \underset{\theta}{\operatorname{argmax}} \sup_{\mathbf{x} \in l_i(\theta)} P_{j \rightarrow i}(\mathbf{x}) \\ &= \underset{\theta}{\operatorname{argmax}} \sup_{\mathbf{x} \in l_j(\theta)} P_j(\mathbf{x}). \end{aligned} \quad (14)$$

This indicates the correspondence lies in epipolar lines induced by the same  $\theta^*$ , i.e.,  $\mathbf{x}_i^* \in l_i(\theta^*)$  and  $\mathbf{x}_j^* \in l_j(\theta^*)$ . Since  $l_j(\theta^*) = \mathbf{F} \tilde{\mathbf{x}}_i^*$ ,  $l_i(\theta^*)$  and  $l_j(\theta^*)$  are the corresponding epipolar lines. Therefore, they are in the same epipolar plane, and the reprojection error is zero.  $\square$

## B Cropped Image Correction and Stereo Rectification

We warp the keypoint distribution using stereo rectification. This requires a composite of transformations because the rectification is defined in the full original image. The transformation can be written as:

$$\bar{h} \mathbf{H}_h = \left( \bar{h} \mathbf{H}_{\bar{c}} \right) \left( \bar{c} \mathbf{H}_b \right) \mathbf{H}_r \left( {}^c \mathbf{H}_b \right)^{-1} \left( {}^h \mathbf{H}_c \right)^{-1}. \quad (15)$$

The sequence of transformations takes a keypoint distribution of the network output  $P$  to the rectified keypoint distribution  $\bar{P}$ : heatmap  $\rightarrow$  cropped image  $\rightarrow$  original image  $\rightarrow$  rectified image  $\rightarrow$  rectified cropped image  $\rightarrow$  rectified heatmap.

Given an image  $\mathcal{I}$ , we crop the image based on the bounding box as shown in Figure 8: the left-top corner is  $(u_x, u_y)$  and the height is  $h_b$ . The transformation from the image to the bounding box is:

$${}^c \mathbf{H}_b = \begin{bmatrix} s & 0 & w_x - su_x \\ 0 & s & w_y - su_y \\ 0 & 0 & 1 \end{bmatrix} \quad (16)$$

where  $s = h_c/h_b$ , and  $(w_x, w_y)$  is the offset of the cropped image. It corrects the aspect ratio factor.  $h_c = 364$  is the height of the cropped image, which is the input to the network. The output resolution (heatmap) is often different from the input,  $s_h = h_h/h_c \neq 1$ , where  $h_h$  is the height of the heatmap. The transformation from the cropped image to the heatmap is:

$${}^h \mathbf{H}_c = \begin{bmatrix} s_h & 0 & 0 \\ 0 & s_h & 0 \\ 0 & 0 & 1 \end{bmatrix} \quad (17)$$

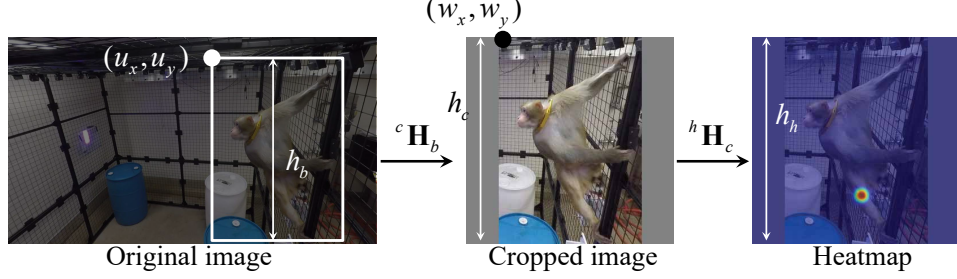


Figure 8: A cropped image is an input to the network where the output is the keypoint distribution. To rectify the keypoint distribution (heatmap), a series of image transformations need to be applied.

The rectified transformations  $(\bar{h}\mathbf{H}_{\bar{c}})$  and  $(\bar{c}\mathbf{H}_{\bar{b}})$  can be defined in a similar way.

The rectification homography can be computed as  $\mathbf{H}_r = \mathbf{K}\mathbf{R}_n\mathbf{R}^\top\mathbf{K}^{-1}$  where  $\mathbf{K}$  and  $\mathbf{R} \in SO(3)$  are the intrinsic parameter and 3D rotation matrix and  $\mathbf{R}_n$  is the rectified rotation of which x-axis is aligned with the epipole, i.e.,  $\mathbf{r}_x = \frac{\mathbf{C}_j - \mathbf{C}_i}{\|\mathbf{C}_j - \mathbf{C}_i\|}$  where  $\mathbf{R}_n = \begin{bmatrix} \mathbf{r}_x^\top \\ \mathbf{r}_y^\top \\ \mathbf{r}_z^\top \end{bmatrix}$  and other axes can be computed by the Gram-Schmidt process.

The fundamental matrix between two rectified keypoint distributions  $\bar{P}_i$  and  $\bar{P}_j$  can be written as:

$$\begin{aligned} \mathbf{F} &= \mathbf{K}_j^{-\top} \begin{bmatrix} 1 \\ 0 \\ 0 \end{bmatrix}_{\times} \mathbf{K}_i^{-1} \\ &= \begin{bmatrix} 0 & 0 & 0 \\ 0 & 0 & 1/f_y^j \\ 0 & 1/f_y^i & -p_y^j/f_y^j - p_y^i/f_y^i \end{bmatrix} \end{aligned} \quad (18)$$

where  $[\cdot]_{\times}$  is the skew symmetric representation of cross product, and

$$\mathbf{K}_i = \begin{bmatrix} f_x^i & 0 & p_x^i \\ 0 & f_y^i & p_y^i \\ 0 & 0 & 1 \end{bmatrix}. \quad (19)$$

This allows us to derive the re-scaling factor of  $a$  and  $b$  in Equation (8):

$$a = \frac{s^i f_y^i}{s^j f_y^j} \quad (20)$$

$$b = s_h s^i \left( \left( \bar{u}_y^j - p_y^j \right) \frac{f_y^i}{f_y^j} + p_y^i - \bar{u}_y^i \right) \quad (21)$$

where  $\bar{u}_y^i$  is the bounding box offset of the rectified coordinate.

## C Evaluation Dataset

All cameras are synchronized and calibrated using structure from motion [8]. The input of most pose detector models except for [1] is a cropped image containing a subject, which requires specifying a bounding box. We use a kernelized correlation filter [58] to reliably track a bounding box using multiview image streams given initialized 3D bounding box from the labeled data.

Subjects	$P$	$ \mathcal{D}_L $	$ \mathcal{D}_U $	$ \mathcal{D}_L / \mathcal{D}_U $	$C$	FPS	Camera type
Monkey	13	85	63,000	0.13%	35	60	GoPro 5
Humans	14	30	20,700	0.14%	69	30	FLIR BlackFly S
Dog I	12	100	138,000	0.07%	69	30	FLIR BlackFly S
Dog II	12	75	103,500	0.07%	69	30	FLIR BlackFly S
Dog III	12	80	110,400	0.07%	69	30	FLIR BlackFly S
Dog IV	12	75	103,500	0.07%	69	30	FLIR BlackFly S

Table 2: Summary of multi-camera dataset where  $P$  is the number of keypoints,  $C$  is the number of cameras,  $|\mathcal{D}_L|$  is the number of labeled data, and  $|\mathcal{D}_U|$  is the number of unlabeled data.